CARBON 76 (2014) 165–174

Available at www.sciencedirect.com

ScienceDirect

journal homepage: www.elsevier.com/locate/carbon

Predicting capacity of hard carbon anodes in sodium-ion batteries using porosity measurements

Clement Bommier [a], Wei Luo [a], Wen-Yang Gao [c], Alex Greaney [b], Shengqian Ma [c], Xiulei Ji [a,*]

[a] Department of Chemistry, Oregon State University, Corvallis, OR 97331, USA
[b] Department of Mechanical, Industrial and Materials Engineering, Oregon State University, Corvallis, OR 97331, USA
[c] Department of Chemistry, University of South Florida, Tampa, FL 33620, USA

ARTICLE INFO

Article history:
Received 28 November 2013
Accepted 19 April 2014
Available online 29 April 2014

ABSTRACT

We report an inverse relationship between measurable porosity values and reversible capacity from sucrose-derived hard carbon as an anode for sodium-ion batteries (SIBs). Materials with low measureable pore volumes and surface areas obtained through N_2 sorption yield higher reversible capacities. Conversely, increasing measurable porosity and specific surface area leads to sharp decreases in reversible capacity. Utilizing a low porosity material, we thus are able to obtain a reversible capacity of 335 mAh g^{-1}. These findings suggest that sodium-ion storage is highly dependent on the absence of pores detectable through N_2 sorption in sucrose-derived carbon.

1. Introduction

In the coming years, research and development of new energy technologies will be an essential part of meeting rising electricity demand while offsetting growing environmental concerns. There are two concurrent priorities in this effort: a drive towards renewable energy generation combined with an inexpensive and large-scale electricity energy storage (EES). The state-of-the-art EES system currently available is lithium-ion batteries (LIBs) [1]. Though they offer high reversibility and efficiency, they are also very expensive due to the rarity and high extraction costs of lithium metal. This is where sodium-ion batteries (SIBs) present themselves as a feasible alternative [2]. They share many similar properties with LIBs, but are much more economically advantageous due to the low cost of sodium, as it is the 6th most abundant element in Earth's crust and can easily be mined from abundant sources. This renders it 95% cheaper than Lithium [3].

However, the size difference between the two ions, 95 pm for Na^+ versus 68 pm for Li^+, makes it such that the technologies of LIBs and SIBs are not always interchangeable. This is especially true when considering the anode material. Unlike LIBs, SIBs cannot use graphitic materials for anodes. It has been well documented that intercalation of Na^+ in graphite is unfavorable [4,5]. Whereas in the rocking-chair model of LIBs, the graphitic anode possesses the chemical formula of LiC_6 after intercalation, its SIB counterpart has a chemical -cformula of NaC_{70} [6]. This has led to significant efforts aimed

* Corresponding author.
E-mail address: david.ji@oregonstate.edu (X. Ji).
http://dx.doi.org/10.1016/j.carbon.2014.04.064
0008-6223/

towards developing a suitable SIB anode. A variety of options have been explored, including carbon materials [7–10], phosphorous [11,12], organic compounds [13], metal oxides [14–16], metal nitrides [17], sodium ternary compounds [18–22], thin film anodes [23] as well as various types of alloys [24–30]. Of the above candidates, carbon-based materials have distinguished themselves as a promising solution as they are cheap, easily attainable and non-toxic. Various types have been investigated such as carbon black [31], carbon microspheres [32], hierarchically porous carbon [33], nitrogen-doped carbons [34,35] graphene nanocomposites [36] and nanostructures [37,38]. While all these materials have their various merits, much interest still remains in the research disordered graphitic carbon—otherwise known as hard carbon.

In previous studies, hard carbon has demonstrated a stable cycling capacity of 285 mAh g^{-1} and 300 mAh g^{-1} by Alcántara et al. [31] and Dahn et al. [10], respectively, and has lately managed to surpass 300 mAh g^{-1} for over 100 cycles as reported by Palacin et al. [39]. The widely-accepted theory suggests that hard carbon can effectively store sodium ions in the nanopores that stem from its randomly scattered graphene nanodomains — this is otherwise known as the 'falling-card' model [9]. This concept leads us to investigate whether a greater nanoporosity will be more effective for sodium-ion storage, which would thus result in a higher reversible capacity.

Herein, we demonstrate a model that strongly suggests reversible capacity of SIBs is inversely proportional to increases in both pore volume and surface area of the hard carbon active material. By reducing the measurable porosity, we report one of the highest reversible capacities to date of hard carbon at 335 mAh g^{-1}.

2. Experimental section

2.1. Materials synthesis and characterizations

The active hard carbon material used in this study is derived from sucrose (Macron Chemicals). Sucrose is dehydrated for 24 h under atmospheric conditions at 180 °C. Chunks of the resulting material are pyrolysed under continuous argon gas flow in a tube furnace for 6 h. The pyrolysis was done at 800 °C, 900 °C, 1000 °C and 1100 °C, with a heating rate of 5 °C min^{-1}. CO_2 activation was performed on samples pyrolysed at 1000 °C at temperatures of 700 °C, 800 °C and 900 °C for durations of 1 h, 2 h, 5 h and 10 h with a heating rate of 10 °C min^{-1} and a CO_2 flow rate of 100 cm^3 min^{-1}. Following the synthesis of the hard carbon material, it was characterized with X-ray diffraction (XRD) using a Rigaku Ultima IV Diffractometer operating at 40 kV and 40 mA using Cu Kα radiation (λ = 1.5406 Å) and a WITec confocal Raman Spectroscopy with a 514 nm laser. Surface morphology was obtained through a FEI Quanta 600 SEM. Surface area was obtained through the Brunauer–Emmett–Teller model (BET) and pore volume was obtained through Density Functional Theory (DTF) using N_2 sorption with a Micromeritics ASAP 2020 Surface Area Analyzer. Elemental analyses were performed on the samples pyrolysed at different temperatures by the Environmental Division of ALS Global.

2.2. Electrochemical measurements

Electrodes were made using a 7:2:1 weight ratio of hard carbon, Super-P carbon black (TimCal) and poly-1,1-difluoroethene (PVDF) binder, respectively. This was mixed in an n-methyl-2-pyrrodilinone (NMP) solvent before being doctor-bladed onto copper foil. Once the anodes were prepared they were punched into disks with loading masses typically between 1.5– 1.8 mg cm^{-2} which were then vacuumed and moved into in an argon-filled glove box for coin cell assembly. The coin cells were composed of a solid sodium metal counter electrode, a glass-fiber separator (PALL) and a 1.0 M $NaClO_4$ electrolyte solution dissolved in a 1:1 weight mixture of ethylene carbonate/propylene carbonate (EC/PC). The batteries were galvanostatically cycled on an Arbin BT2000 system at an initial current rate of 40 mA g^{-1}, which translates into a cycling rate of C/8 as we consider 300 mAh g^{-1} to be 1 C. Higher rates from 100 mA g^{-1} to 1 A g^{-1} were used to investigate the rate capability of the materials. At a current rate of 40 mA g^{-1} carbon black has a reversible capacity of 150 mAh g^{-1}, which is included in the supplementary section (Fig. S1). Since our electrodes comprise 20 weight% of carbon black, this would represent a capacity contribution of 30 mAh g^{-1}. Erring on the side of caution, we removed 40 mAh g^{-1} of capacity at a current rate of 40 mA g^{-1}, which gives us the reversible capacity of 335 mAh g^{-1}.

Cyclic voltammetry was performed on a VMP-3 multichannel workstation at a scanning rate of 0.2 mV s^{-1} at room temperature. Statistical modeling data was obtained through the R programming package.

3. Results and discussion

We pyrolysed sucrose at 1000 °C for preparation of the hard carbon. We first tested whether increasing porosity via CO_2 activation would lead to higher capacities. The CO_2 activation can be described by the following reaction:

$$C(s) + CO_2(g) \rightarrow 2CO(g) \quad (1)$$

This reaction consumes part of the solid carbon, thereby increasing its porosity and surface area. Samples were initially activated at a temperature of 900 °C, with reaction durations of 1 h, 2 h, 5 h and 10 h (Table 1). Half cells were then made from the activated carbons and characterized by galvanostatic charge/discharge cycling (Fig. 1a). The capacities reported are those obtained during the desodiation process of the anode, often referred to as reversible capacity, and are solely attributed to the sucrose-derived hard carbon. An activated sample is referred to as 'T °C-n h' if it was treated at T °C for n hours.

The unactivated sample has an initial reversible capacity of 290 mAh g^{-1}. After activation of 1 h and 2 h, the capacities drop to 239 mAh g^{-1} and 208 mAh g^{-1}, respectively. The samples that were activated for 5 h and 10 h exhibit even lower reversible capacities of 120 mAh g^{-1} and 49 mAh g^{-1}, respectively. It is evident that CO_2 activation at 900 °C decreases reversible capacity, with longer activation durations yielding progressively worse results. We hoped that milder activation temperatures of 700 °C and 800 °C would be more conducive to forming the desired nanopores, and offer an improvement

Table 1 – Measurable pore volume/surface area data and capacities for samples obtained through CO_2 activation.

CO_2 activation temperature/ time	DFT Pore Volume ($cm^3\ g^{-1}$)	BET Surface Area ($m^2\ g^{-1}$)	abs (ln DFT Pore Volume)	ln surface area	1st cycle reversible capacity ($mAh\ g^{-1}$)	Irreversible capacity (%)
Untreated	0.042	58.7	3.16	4.07	282.9	28.6
Untreated	0.042	58.7	3.16	4.07	290.4	21.0
900 °C-1 h	0.177	219.6	1.73	5.39	239.3	33.5
900 °C-1 h	0.177	219.6	1.73	5.39	214.9	22.2
900 °C-2 h	0.265	340.6	1.33	5.83	208	45.0
900 °C-2 h	0.265	340.6	1.33	5.83	186.5	54.9
900 °C-5 h	0.607	832.5	0.50	6.72	107.1	71.9
900 °C-5 h	0.607	832.5	0.50	6.72	120.7	75.7
900 °C-10 h	0.908	1410.3	0.10	7.25	49.3	80.8
900 °C-10 h	0.908	1410.3	0.10	7.25	43.6	89.9
800 °C-1 h	0.082	102.6	2.51	4.63	257.4	29.1
800 °C-1 h	0.082	102.6	2.51	4.63	229.6	32.9
800 °C-2 h	0.126	154.4	2.07	5.04	240.6	31.2
800 °C-2 h	0.126	154.4	2.07	5.04	236.6	32.0
800 °C-5 h	0.123	155.4	2.09	5.05	221.7	23.9
800 °C-5 h	0.123	155.4	2.09	5.05	218.5	44.0
800 °C-10 h	0.197	256.9	1.62	5.55	268.3	28.9
800 °C-10 h	0.197	256.9	1.62	5.55	228.9	37.0
700 °C-1 h	0.122	152.1	2.10	5.02	232.5	25.6
700 °C-1 h	0.122	152.1	2.10	5.02	225.3	34.3
700 °C-2 h	0.094	126.4	2.37	4.84	205.8	32.7
700 °C-2 h	0.094	126.4	2.37	4.84	192.7	45.8
700 °C-5 h	0.099	141.9	2.31	4.95	263.5	21.4
700 °C-5 h	0.099	141.9	2.31	4.95	255.1	29.5
700 °C-10 h	0.140	196.5	1.97	5.28	249.8	25.1
700 °C-10 h	0.140	196.5	1.97	5.28	241.5	25.3

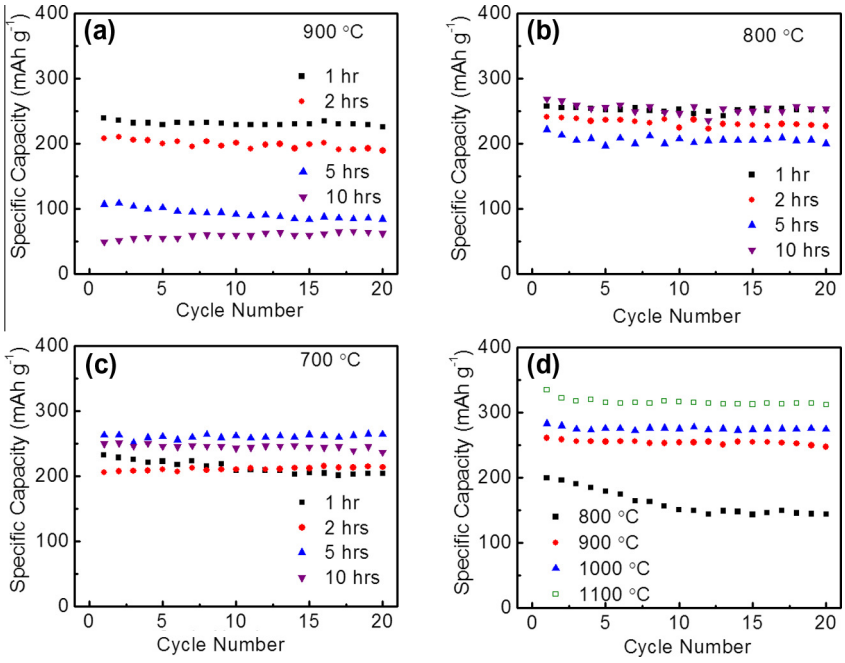

Fig. 1 – Initial cycling performance at 40 mA g^{-1} for carbons activated (a) 900 °C (b) 800 °C (c) 700 °C for different durations and (d) initial cycling performance of carbons pyrolysed at different temperatures. (A colour version of this figure can be viewed online.)

over those obtained at 900 °C. However, these lower temperatures also caused a decrease in reversible capacity (Fig. 1b and c). Interestingly, longer activation durations at lower temperatures do not necessarily lead to lower capacities. Contrary to what had been observed at 900 °C, the 700 °C-2 h activated carbon shows an initial reversible capacity of 206 mAh g^{-1}, the lowest of the 700 °C series, while the 700 °C-5 h has the highest reversible capacity at 264 mAh g^{-1}.

Seeing losses in capacity following CO_2 activation led us to search for a link between the physical properties of the materials and their sodium-ion storage performance. XRD patterns and Raman spectra were collected for the untreated carbon and its CO_2 activated counterparts (Fig. 2a and b and Fig. S2). All the samples obtained demonstrate the typical characteristics of amorphous carbon: broad peaks at 24° and 43°, representing the (002) and (100) planes, respectively. The 900 °C-5 h and 900 °C-10 h samples exhibit even less resolved XRD peaks, indicating a disruption of the amorphous structure by activation. Raman spectra were inconclusive as well. The intensity ratios (I_d/I_g) of the D-band (1350 cm^{-1}) representing the defected sp^2 hybridized carbon over the G-band (1580 cm^{-1}) measuring the sp^2 hybridized carbon show little variation (Table S1). An I_d/I_g greater than 1 indicates a more disordered carbon.

On the other hand, Density Functional Theory (DFT) pore volume and Brunauer–Emmett–Teller (BET) surface area, calculated through N_2 sorption measurements, show dramatic changes following CO_2 activation. All activated samples exhibit greater measurable pore volume and surface area than the untreated control. The roughened surface morphology is

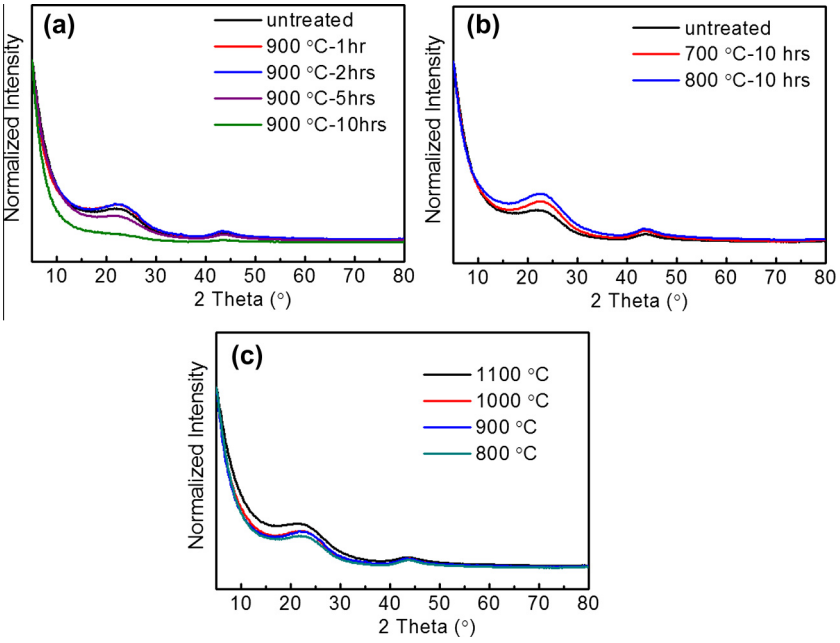

Fig. 2 – XRD patterns of different samples. (a) Samples after CO_2 activation at 900 °C for different durations. (b) Samples of 700 °C-10 h and 800 °C-10 h. The untreated sample in (a) and (b) is the hard carbon pyrolysed at 1000 °C. (c) Sucrose-derived hard carbon pyrolysed at different temperatures, unactivated. (A colour version of this figure can be viewed online.)

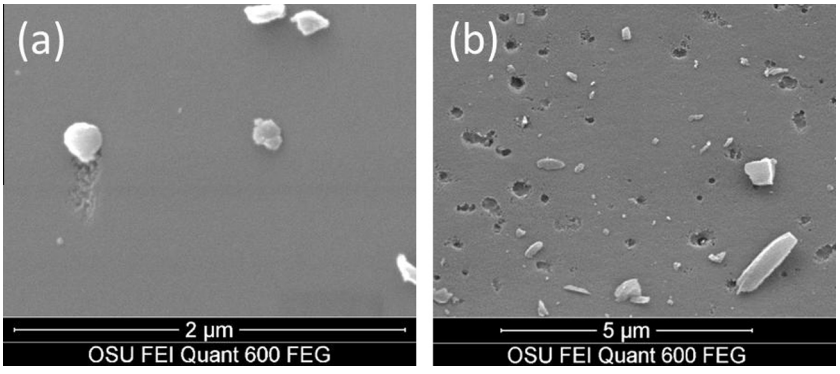

Fig. 3 – SEM images showing that activation roughens surface morphology of sucrose-derived carbon (a) pyrolysed at 1000 °C, unactivated, (b) pyrolysed at 1000 °C and activated under CO_2 at 900 °C for 10 h. Mesopores (2–50 nm) and micropores (less than 2 nm) are not observable at such low magnification.

evident from the SEM images (Fig. 3a and b). Higher CO_2 activation temperatures and/or longer reaction times give rise to larger pore volume and surface area. For example, the 900 °C-10 h sample yields a surface area of 1410.3 $m^2 g^{-1}$ and a pore volume of 0.91 $cm^3 g^{-1}$, comparing to a pore volume of 0.042 $cm^3 g^{-1}$ and a surface area of 58.7 $m^2 g^{-1}$ for the unactivated material (Table 1).

We then plotted the first reversible capacity of all the samples as a function of their measurable specific pore volume and surface area (Fig. 4). When a linear regression analysis was performed, the data yields coefficient of determination values (R^2) of 0.889 for the pore volume plot and of 0.879 for the surface area plot. To minimize the bias from the outlying data points from 900 °C-5 h and 900 °C-10 h, while spreading out the clustered ones, we performed a natural logarithm (ln) transform of the pore volume and surface area values. As the pore volumes were quantities smaller than one for all samples, we further took the absolute value (abs) to avoid negative values. The consequent R^2 results obtained are 0.793 and 0.810 for the pore volume and surface area plots, respectively. Both models demonstrate that reversible capacity is inversely proportional to DFT Pore Volume and surface area.

Following the CO_2 activation, we tried to gauge the effect that different sucrose pyrolysis temperatures would have on the active material. For this, we utilized temperatures of 800 °C, 900 °C and 1100 °C compared to the 1000 °C used for our original material.

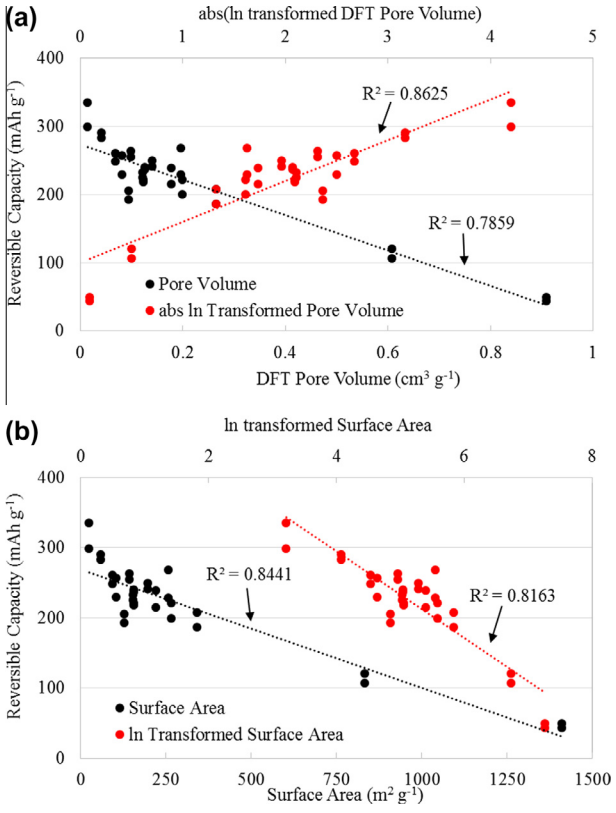

Fig. 4 – Linear and natural logarithm transformed models plotting the reversible capacity in the 1st cycle as a function of (a) DFT specific pore volume (b) BET specific surface area. The best and worst results for the same materials were plotted. (A colour version of this figure can be viewed online.)

Once again, the reversible capacities are closely related to porosity values. The material obtained at 1100 °C has the lowest measurable pore volume and surface area, 0.015 $cm^3 g^{-1}$ and 24.8 $m^2 g^{-1}$, of the all samples obtained. It yields an initial reversible capacity of 335 mAh g^{-1} with the contribution of super-P carbon taken out. Conversely, the sample pyrolysed at 800 °C has the highest pore volume and surface area of the series at 0.199 $cm^3 g^{-1}$ and 265.8 $m^2 g^{-1}$, respectively, and only achieved a reversible capacity of 200 mAh g^{-1} (Table 2).

When the data points from the different pyrolysis temperatures were added to the plots, the R^2 values stay relatively constant: 0.862 for the DFT Pore Volume model and 0.844 for the Surface Area model. The R^2 for the ln transformed models is also unchanged, standing at 0.786 for the ln DFT Pore Volume model and 0.816 for the ln Surface Area model (Fig. 4). Looking at the results of the regression analyses performed, all of the *p*-values obtained, with 30 degrees of freedom (DF), are below $1.5 \cdot 10^{-11}$. A *p*-value is the probability of obtaining a test statistic (e.g. R^2) equal to or greater than one obtained at random. A *p*-value of less than 0.05 is considered statistically significant. This proves that there is very strong evidence linking reversible capacity to DFT Pore Volume and Surface Area (Fig. S3).

We are aware that it is possible that impurities in pyrolysed carbon can have an impact on the Na^+ ion storage. Elemental analyses for the carbons obtained at different pyrolysis temperatures were conducted. All the materials tested have carbon ranging from 93 to 97 mass% and hydrogen from 0.2 to 0.6 mass% with the rest as oxygen (Table S2). Our data are expected as it was reported that pyrolysis of cellulose, as a polymer of sucrose, occurs well below 800 °C with mainly carbon as the composition [40]. It is evident now the very much different capacities from the materials pyrolysed at various temperatures were obtained at the similar levels of extraneous hydrogen and oxygen residues. Such a vast capacity variations can be only attributed to the porosity differences between these samples.

As was the case with the CO_2 activation samples, the XRD profiles and Raman spectroscopy data obtained from the samples pyrolysed at different temperatures varied little. The XRD patterns all exhibit the (002) and (100) peaks, while the I_d/I_g ratios obtained from Raman spectra range narrowly from 0.97 to 1.04 (Fig. 2c, Fig. S2, and Table S1).

Considering that N_2 can only be adsorbed in pores approximately equal to or larger than ~0.4 nm [41], we can infer from the models that Na^+-ion storage in hard carbon is highly dependent on the absence of such open pores. This leads us to classify the carbon atoms that contribute to the surface area and porosity as 'exposed carbon atoms'. The percentage of 'exposed carbon atoms' is available through the equation:

$$\frac{A_t/2\pi r^2}{N_A/MM} \quad (2)$$

where A_t represents the measured BET Surface Area, and *r* is the radius of a carbon atoms; *MM* and N_A, are the Molar Mass and Avogadro's number, respectively.

Table 2 – Measureable pore volume/surface area data and capacities for samples obtained at different pyrolysis temperatures.

Pyrolysis temperature (°C)	DFT Pore Volume ($cm^3\ g^{-1}$)	BET surface area ($m^2\ g^{-1}$)	abs (ln DFT Pore Volume)	ln surface area	1st cycle reversible capacity (mAh g^{-1})	Irreversible capacity (%)
800	0.199	265.8	1.61	5.58	199.8	34.0
800	0.199	265.8	1.61	5.58	221.4	23.4
900	0.069	92.8	2.68	4.53	260.9	24.0
900	0.069	92.8	2.68	4.53	248.2	14.3
1000	0.042	58.7	3.16	4.07	282.9	28.6
1000	0.042	58.7	3.16	4.07	290.4	21.0
1100	0.015	24.8	4.19	3.21	335.0	4.4
1100	0.015	24.8	4.19	3.21	299.0	20.3

We assume that an exposed carbon atom contributes to measurable surface area with a single hemisphere, whose area is equal to $2\pi r^2$ with r equal to 0.73 Å, the half of the bond length of adjacent carbon atoms in the graphene sheet. We can estimate ratio between the exposed carbon atoms in numerator and the total number of atoms in the denominator.

We then used this to calculate for the percentage of unexposed carbon atoms by using the equation:

$$\%\ \text{Unexposed carbon atoms} = 1 - \%\ \text{exposed carbon atoms} \quad (3)$$

Using this metric it was found that the material exhibiting the lowest reversible capacity had only 8.7% of unexposed carbon atoms, while the best performing material had 98.4% unexposed carbon atoms. Plotting the values of reversible capacity vs. logit transform of the percentage of the unexposed carbon atoms yields an R^2 value of 0.89 with a p-value of $6.3 \cdot 10^{-16}$ on 30 DF (Fig. 5 and Fig. S4). This suggests that, unlike unexposed atoms, exposed carbon atoms have inferior contributions towards Na^+-ion storage. This may be due to the fact that the exposed carbon atoms tend to act as nucleation sites for solid electrolyte interphase (SEI), a passivation layer that stems from the decomposition of the electrolyte solvents or salts. This passivation layer may disable the Na^+-ion storage on the electrode surface due to its electronically-insulating nature and block the access of Na^+ ions to the enclosed voids inside the carbon structure.

Evidence of the greater SEI formation on high surface area material can be seen through a comparison of electrochemical impedance spectroscopy (EIS) measurements. These were taken at various voltages in the course of the initial discharge. The low-surface-area carbon (24 $m^2\ g^{-1}$), referred to as lowSAC, has the larger initial semi-circle, indicating a higher resistivity for interface charge transfer. However, once the batteries have been fully discharged at 0.01 V, the high surface area carbon (1410 $m^2\ g^{-1}$), referred to as highSAC, exhibits a much larger semi-circle than the lowSAC (Fig. 6). Further proof of the difference in SEI formation is seen when comparing the 1st and 2nd cycle CV curves of highSAC and lowSAC. Since the bulk of SEI formation occurs in the first cycle, the area enclosed by the CV curve during the 2nd cycle is expected to drop as there will be a less significant formation of the passivation layer. When comparing the enclosed areas, the highSAC showed a 26% decrease of the enclosed area from the first to the second cycle, while the lowSAC only showed a 6% decrease (Fig. S5 and Table S4). Moreover, there

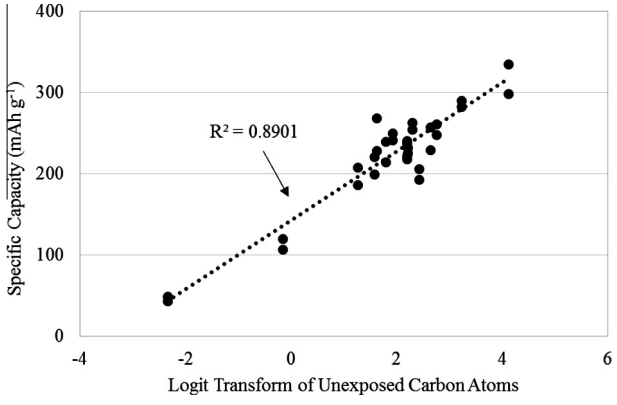

Fig. 5 – Reversible capacity vs. logit transform of the percentage of the unexposed carbon atoms. The logit transform takes the formula of: $\ln \frac{\%\ \text{unexposed carbon atoms}}{1-\%\ \text{unexposed carbon atoms}}$. This allows for a greater spread of percentage values on the x-axis.

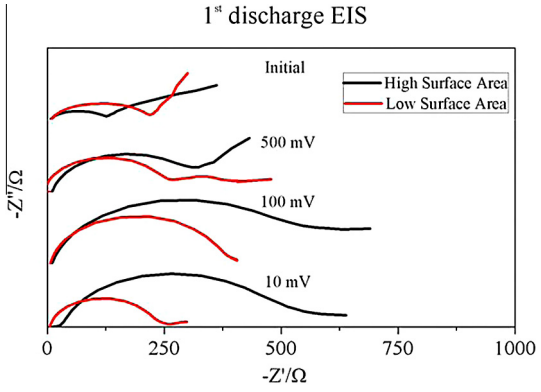

Fig. 6 – A comparison of Nyquist plots of electrochemical impedance spectroscopy results of high (1410 $m^2\ g^{-1}$) and low (24 $m^2\ g^{-1}$) surface area carbon materials as electrodes. The measurements were taken ex-situ at various stages during the first discharge. The plots at the same voltages from high-surface-area and low-surface-area electrodes have been superimposed for clarity. (A colour version of this figure can be viewed online.)

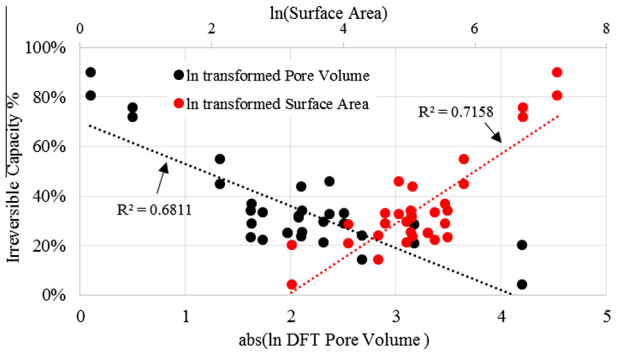

Fig. 7 – Natural logarithm (ln) transformed models comparing irreversible capacity percentage of the first cycle versus absolute value of ln pore volume and ln surface area. The best and worst results for the same materials were ploted. (A colour version of this figure can be viewed online.)

is no oxidation peak in the anodic scan associated to the sodium-metal oxidation with the highSAC, which indicates that, besides the SEI formation, even the deposited sodium metal or ions in the nanopores of highSAC are not electrochemically removable. This is partially responsible to the low capacity of high surface materials. In summary, both the EIS and CV measurements support that more SEI was formed with the high surface area material. Similar phenomenon has been observed on higher-surface-area carbon materials in Li-ion batteries [7].

It is also well known that SEI formation causes irreversible capacity during the first cycle and is proportional to the measurable surface area of carbon materials [42,43]. To confirm this, we plotted the percentage of irreversible capacity over the discharge capacity in the first cycle vs. the ln transformed pore volume and surface area for all the samples (Fig. 7). A linear regression analysis yields reasonable R^2 values. Both corresponding p-values, obtained with 30 DF, are below $7 \cdot 10^{-9}$, thereby implying that there is strong evidence linking irreversible capacity with DFT Pore Volume and Surface Area (Fig. S6).

We further investigated the electrochemical properties of the two materials. The charge/discharge profiles differ greatly between lowSAC and highSAC. The former displays two distinct features during desodiation. The first is a relatively flat plateau that runs from 0.05 V to 0.2 V. This is followed by a sloping curve to 2.0 V. The flat plateau of the desodiation curve can be attributed to the de-insertion of the sodium ions from voids between graphite nanodomains. The sloping curve stems from the sodium-ion de-intercalation out of graphite nanocrystals. The latter eschews these characteristics. Instead it exhibits a capacitor-like behavior where the voltage rises almost linearly from 0.01 V to 2.0 V during the same desodiation process (Fig. 8a and b) [9].

The lower reversible capacity for high surface area materials is clearly associated with the loss of capacity obtained below ~0.2 V. This portion of capacity can be attributed to the de-insertion of Na^+ ions from voids inside the closed hard carbon structure according to the hypothesis by Dahn and Stevens [6,9]. With higher porosity generated, such closed hard carbon structure has been destroyed, which is responsible for the observed loss of capacity at low voltage, e.g. below 0.2 V. The capacity obtained at higher than 0.2 V may be from either the de-intercalation of ions from graphitic structures or electrical double layer capacitance [9,44]. In order to quantify the loss of capacity at low voltages, a ratio of the reversible capacity under 0.2 V over the total reversible capacity was calculated (Table S5).

When comparing these ratios to the respective measurable specific surface areas, we discovered that low surface area materials typically obtain around 50% of their reversible capacity below 0.2 V. On the other hand, higher surface area materials, notably the 900 °C-5 h and 900 °C-10 h samples, obtain only ~10% of their reversible capacity under 0.2 V. The aforementioned ratio vs. surface area was plotted and fitted with a linear regression model that yields an R^2 value of 0.831 and a p-value of $4.2 \cdot 10^{-13}$ (Fig. S7). When increasing open porosity of hard carbon, the volume of the closed hard carbon structure conducive for Na^+ storage is certainly diminished. This is why the capacity is inversely proportional to the specific pore volume/surface area.

Cyclic voltammetry (CV) was conducted at a scanning rate of 0.2 mV s^{-1} for lowSAC. During the initial cathodic scan, there is a broad reduction plateau between 0.2 and 0.6 V, indicative of SEI formation. The CV curves have sharp reduction and oxidation peaks between 0.01 V and 0.2 V. The reduction peak is attributed to insertion of Na^+ into the voids in hard carbon, while the oxidation peak signifies their removal

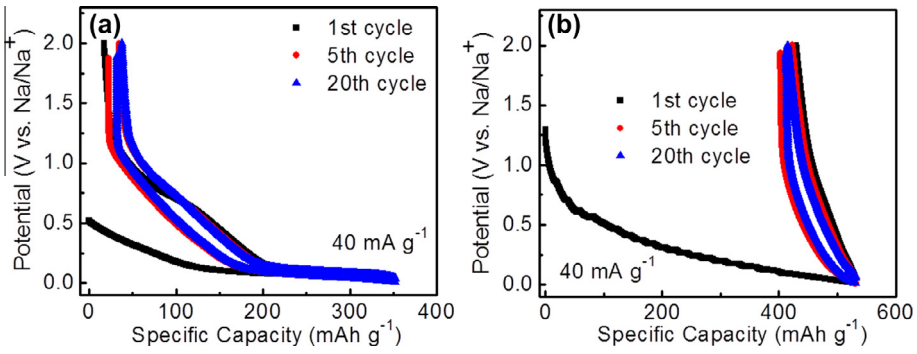

Fig. 8 – (a) Galvanostatic charge-discharge profiles of lowSAC, carbon pyrolysed at 1100 °C, unactivated, (b) charge-discharge profiles of highSAC, carbon pyrolysed at 1000 °C and activated at 900 °C for 10 h. (A colour version of this figure can be viewed online.)

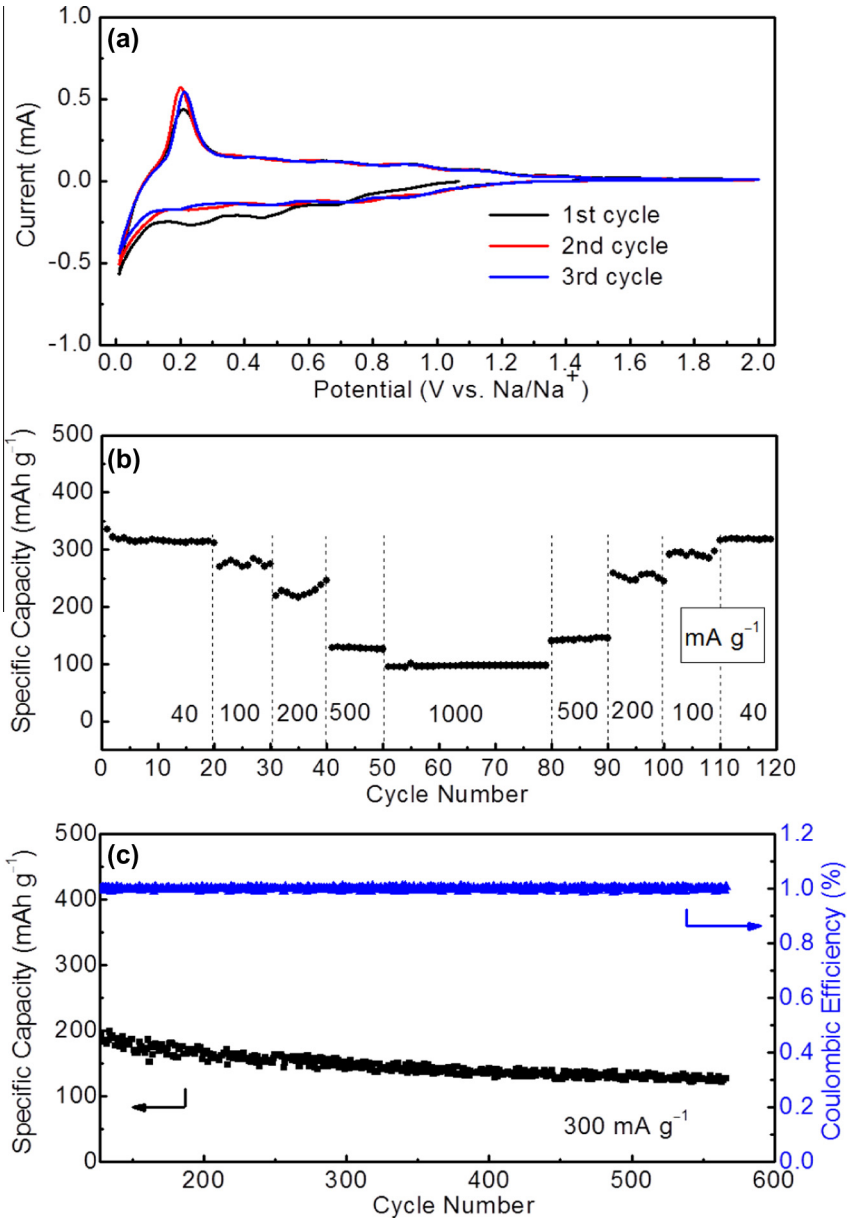

Fig. 9 – Electrochemical characterizations of C-1100. (a) CV curves for the first three cycles at a scanning rate of 0.2 mV s^{-1}, (b) galvanostatic cycling at different current rates, (c) long term galvanostatic cycling at a high rate of 300 mA g^{-1}. (A colour version of this figure can be viewed online.)

(Fig. 9a) [29]. These results agree well with the charge/discharge profiles, as the charge and discharge curve plateau when the voltage is below 0.2 V. CV was also conducted on the highSAC, but it was found that the oxidation peak associated to sodium-metal oxidation in the anodic scan occurring between 0.01 and 0.2 V had mostly vanished (Fig. S5). Instead, the CV curve for the high surface area material begins to adopt the characteristics of a capacitor. This corroborates what was seen in the charge/discharge curves as well as the observation that increased surface area and porosity lead to a decrease of Na^+ ion storage features, which leads to the loss of reversible capacity obtained at voltages below 0.2 V.

We also investigated the cycling performance of the C-1100 with different current rates (Fig. 9b). Decreases in specific capacity are observed at higher currents, though this is expected due to the kinetic limitation of hard carbon. After 100 cycles, the carbon material showed almost no loss in capacity at 40 mA g^{-1} when compared to the capacities of the initial cycles. A long term cycling at 300 mA g^{-1} was also conducted, and after 500 cycles, 70% of the initial capacity remained (Fig. 9c).

4. Conclusion

We demonstrate that there is an inherent relationship between the porosity and reversible capacity: increases of measurable porosity are very strongly associated with lower reversible capacities. This insight may be applied to other

bio-mass converted hard carbons as anodes in SIBs, as it reveals that superior Na^+ ion storage in such batteries is dependent on the absence of pores detectable through N_2 sorption. Using a low measurable surface area/porosity hard carbon we are able to achieve a reversible capacity of 335 mAh g^{-1} at a current rate of 40 mA g^{-1} along with a relatively stable long term cycling (500 cycles) at 300 mA g^{-1}. In our laboratories, there are ongoing efforts in search of yet lower pore volumes aimed for further increasing energy density while lowering irreversible capacity.

Acknowledgements

X.J. gratefully acknowledges the financial support from Advanced Research Projects Agency-Energy (ARPA-E), Department of Energy of the United States, Award Number: DE-AR0000297TDD. We thank Dr. Jong-Jan Lee, Dr. Yuhao Lu, Dr. Sean Vail and Dr. Long Wang from Sharp Labs America for their suggestions and assistance. The authors would like to thank Dr. Peter Eschbach and Ms. Teresa Sawyer for the SEM measurements in OSU EM Facility funded by National Science Foundation, the Murdock Charitable Trust and the Oregon Nanoscience and Microtechnology Institute. We appreciate Professor Chih-Hung Chang and Mr. Changqing Pan for Raman spectra studies. Lastly, we are grateful to Professor Michael M. Lerner for his advice.

Appendix A. Supplementary data

Supplementary data associated with this article can be found, in the online version, at http://dx.doi.org/10.1016/j.carbon.2014.04.064.

REFERENCES

[1] Wang L, Lu Y, Liu J, Xu M, Cheng J, Zhang D, et al. A superior low-cost cathode for a na-ion battery. Angew Chem Int Ed 2013;52:1964.
[2] Dunn B, Kamath H, Tarascon JM. Electrical energy storage for the grid: a battery of choices. Science 2011;334:928.
[3] Slater MD, Kim D, Lee E, Johnson CS. Sodium-ion batteries. Adv Funct Mater 2011;23:947–9.
[4] Udod IA, Orman HB, Genchel VK. The sodium-graphite system under high-pressure conditions: the comparison with the lithium-graphite system. Carbon 1994;32:101–5.
[5] Avdeev VV, Nalimova VA, Semenenko KN. Sodium-graphite system at high pressures. Synth Met 1990;38:363–9.
[6] Stevens DA, Dahn JR. The mechanisms of lithium and sodium insertion in carbon materials. J Electrochem Soc 2001;148:A805.
[7] Komaba S, Murata W, Ishikawa T, Yabuuchi N, Ozeki T, Nakayama T, et al. Electrochemical Na insertion and solid electrolyte interphase for hard-carbon electrodes and application to Na-ion batteries. Adv Funct Mater 2011;21:2859–63.
[8] Gotoh K, Ishikawa T, Shimadzu S, Yabuuchi N, Komaba S, Takeda K, et al. NMR study for electrochemically inserted Na in hard carbon electrode of sodium ion battery. J Power Sources 2013;225:137.
[9] Stevens DA, Dahn JR. High capacity anode materials for rechargeable sodium-ion batteries. J Electrochem Soc 2000;147:1271.
[10] Xia X, Obravac MN, Dahn JR. Comparison of the reactivity of NaxC6 and LixC6 with non-aqueous solvents and electrolytes. Electrochem Solid-State Lett 2011;14:A130.
[11] Kim Y, Park Y, Choi A, Choi NS, Kim J, Lee J, et al. An amorphous red phosphorus/carbon composite as a promising anode material for sodium ion batteries. Adv Mater 2013;25:3045.
[12] Qian JF, Wu XY, Cao YL, Ai XP, Yang HX. High capacity and rate capability of amorphous phosphorus for sodium ion batteries. Angew Chem Int Ed 2013;52:4633.
[13] Park Y, Shin D, Woo SH, Choi NS, Shin KH, Oh SM, et al. Sodium terephthalate as an organic anode material for sodium ion batteries. Adv Mater 2012;24:3562.
[14] Xiong H, Slater MD, Balasubramanian M, Johnson CS, Rajh T. Amorphous TiO_2 nanotube anode for rechargeable sodium ion batteries. J Phys Chem Lett 2011;2:245.
[15] Alcántra R, Jaraba M, Lavela P, Tirado JT. $NiCo_2O_4$ spinel: first report on a transition metal oxide for the negative electrode of sodium-ion batteries. Chem Mater 2002;14:287.
[16] Bi ZH, Paranthaman MP, Menchhofer PA, Dehoff RR, Bridges CA, Chi MF, et al. Self-organized amorphous TiO_2 nanotube arrays on porous Ti foam for rechargeable lithium and sodium ion batteries. J Power Sources 2013;222:461.
[17] Li X, Hasan MM, Hector AL, Owen JR. Performance of nanocrystalline Ni3N as a negative electrode for sodium-ion batteries. J Mater Chem A 2013;1:6441.
[18] Senguttuvan P, Rousse G, Seznec V, Tarascon JM, Palacin MR. $Na_2Ti_3O_7$: lowest voltage ever reported oxide insertion electrode for sodium ion batteries. Chem Mater 2011;23:4109.
[19] Senguttuvan P, Rousse G, Arroyo y Dompablo ME, Vezin H, Tarascon JM, Palacin MR. Low-potential sodium insertion in a NASICON-type structure through the Ti(III)/Ti(II) redox couple. J Am Chem Soc 2013;135:3897.
[20] Park Y, Shin DS, Woo SH, Choi NS, Shin KH, Oh SM, et al. Sodium terephthalate as an organic anode material for sodium ion batteries. Adv Mater 2012;24:3562.
[21] Zhao L, Zhao JM, Hu YS, Li H, Zhou ZB, Armand M, et al. Disodium terephthalate ($Na_2C_8H_4O_4$) as high performance anode material for low-cost room-temperature sodium-ion battery. Adv Energy Mater 2012;2:962.
[22] Park SI, Gocheva I, Okada S, Yamaki JI. Electrochemical properties of $NaTi_2(PO_4)_3$ anodes for rechargeable aqueous sodium-ion batteries. J Electrochem Soc 2011;158:A1067.
[23] Sun Q, Ren QQ, Li H, Fu ZW. High capacity Sb_2O_4 thin film electrodes for rechargeable sodium battery. Electrochem Commun 2011;13:1462.
[24] Liu Y, Xu Y, Zhu Y, Culver J, Lundgren CA, Xu K, et al. Tin-coated viral nanoforests as sodium-ion battery anodes. ACS Nano 2013;7:3627.
[25] Darwiche A, Marino C, Sougratti MT, Fraise B, Stievano L, Monconduit L. Better cycling performances of bulk Sb in Na-ion batteries compared to Li-ion systems: an unexpected electrochemical mechanism. J Am Chem Soc 2012;134:20805.
[26] Qian JF, Chen Y, Wu L, Cao YL, Ai XP, Yang HX. High capacity Na-storage and superior cyclability of nanocomposite Sb/C anode for Na-ion batteries. Chem Commun 2012;48:7070.
[27] Xu YH, Zhu YJ, Liu YJ, Wang CS. Electrochemical performance of porous carbon/tin composite anodes for sodium-ion and lithium-ion batteries. Adv Energy Mater 2013;3:128.
[28] Wang JW, Liu XH, Mao SX, Huang JY. Microstructural evolution of tin nanoparticles during in situ sodium insertion and extraction. Nano Lett 2012;12:5897.
[29] Datta MK, Epur R, Saha P, Kadakia K, Park SK, Kuma PN. Tin and graphite based nanocomposites: potential anode for sodium ion batteries. J Power Sources 2013;225:316.
[30] Palomares V, Serras P, Villaluenga I, Hueso KB, Carretero-González J, Rojo T. Na-ion batteries, recent advances and

present challenges to become low cost energy storage systems. Energy Environ Sci 2012;5:5884–901.
[31] Alcántara R, Jiménez-Mateos JM, Lavela P, Tirado JL. Carbon black: a promising electrode material for sodium-ion batteries. Electrochem Commum 2001;3:639–40.
[32] Alcántara R, Lavela P, Ortiz GF, Tirado JL. Carbon microspheres obtained from resorcinol-formaldehyde as high-capacity electrodes for sodium-ion batteries. Electrochem Solid-State Lett 2005;8:A222–5.
[33] Wenzel S, Hara T, Janek J, Adelhelm P. Room-temperature sodium-ion batteries: improving the rate capability of carbon anode materials by templating strategies. Energy Environ Sci 2011;4:3342.
[34] Wang ZH, Qie L, Yuan X, Zhang WX, Lu XL, Huang YH. Functionalized N-doped interconnected carbon nanofibers as an anode material for sodium-ion storage with excellent performance. Carbon 2013;55:328.
[35] Wang HG, Wu Z, Meng FL, Ma DL, Huang XL, Wang LM, et al. Nitrogen-doped porous carbon nanosheets as low-cost, high-performance anode material for sodium-ion batteries. ChemSusChem 2013;6:56.
[36] Su D, Ahn HJ, Wang G. SnO_2@graphene nanocomposites as anode materials for Na-ion batteries with superior electrochemical performance. Chem Commun 2013;49:3131.
[37] Tang K, Fu L, White RJ, Yu L. Hollow carbon nanospheres with superior rate capability for sodium-based batteries. Adv Energy Mater 2012;2:873.
[38] Cao YL, Xiao LF, Sushko ML, Wang W, Schwenzer B, Xiao J, et al. Sodium ion insertion in hollow carbon nanowires for battery applications. Nano Lett 2012;12:3783.
[39] Ponrouch A, Goni AR, Rosa Palacin M. Towards high energy density sodium ion batteries through electrolyte optimization. Electrochem Commum 2013;25:85.
[40] Chuan-Lin Y, Cho J, Tompsett GA, Westmoreland PR, Huber GW. Kinetics and mechanism of cellulose pyrolysis. J Phys Chem C 2009;113:20097.
[41] Ravikovitch P, Vishnyakov A, Russo R, Neimark AV. Unified approach to pore size characterization of microporous carbonaceous materials from N_2, Ar, and CO_2 adsorption isotherms. Langmuir 2000;16:2316.
[42] Fong R, Sacken U, Dahn JR. Studies of lithium intercalation into carbons using nonaqueous electrochemical cells. J Electrochem Soc 1990;7:2010.
[43] Winter M, Novak P, Monnier A. Graphite for lithium-ion celles: the correlation of the first-cycle charge loss with the BET surface area. J Electrochem Soc 1998;2:428.
[44] Shao Y, Xiao J, Wang W, Engelhard M, Liu J, et al. Surface-driven sodium ion energy storage in nanocellular carbon foams. Nano Lett 2013;13:3909–10.